MARANGONI CONVECTION AROUND A VENTILATED AIR BUBBLE UNDER MICROGRAVITY CONDITIONS

HOEFSLOOT, HCJ; JANSSEN, LPBM; HOOGSTRATEN, HW

Published in:
Chemical Engineering Science

DOI:
10.1016/0009-2509(94)85031-3

Publication date:
1994

Chemical Engineering Science, Vol. 49, No. 1, pp. 29–39, 1994.
Printed in Great Britain.

0009–2509/94 $6.00 + 0.00

MARANGONI CONVECTION AROUND A VENTILATED AIR BUBBLE UNDER MICROGRAVITY CONDITIONS

H. C. J. HOEFSLOOT,[†] L. P. B. M. JANSSEN[†‡] and H. W. HOOGSTRATEN[§]
Departments of [†]Chemical Engineering and [§]Mathematics, University of Groningen, Groningen, The Netherlands

(*Received* 20 *January* 1992; *accepted for publication* 5 *April* 1993)

Abstract—Under microgravity conditions in both parabolic and sounding rocket flights, the mass-transfer-induced Marangoni convection around an air bubble was studied. To prevent the bubble from becoming saturated, the bubble was ventilated. It turned out that the flow rate of the air through the bubble determined the flow pattern in the liquid. A mathematical model is presented which can adequately describe the observed phenomena.

1. INTRODUCTION

Mass transfer across fluid interfaces plays an important role in process technology. Perturbations in mass transfer can give rise to local changes in surface tension and density, both resulting in convection in the fluid phases. The effects of surface tension will be dominant in thin films, as they occur frequently in process industry, giving rise to Marangoni convection. In thicker films buoyancy effects will determine the flow field and Rayleigh convection will occur. Experiments under microgravity conditions suppress buoyancy effects and provide a good opportunity to investigate phenomena as they occur in thin films under terrestrial circumstances. In due course a thorough understanding of Marangoni convection could lead to modified design rules for mass transfer equipment.

A first series of experiments, performed during the Space-Lab D1 flight in 1985, was aimed at the study of mass-transfer-induced Marangoni convection in a rectangular container (Dijkstra and Lichtenbelt, 1988). The container was partially filled with a 3% acetone in water solution, the acetone evaporating from the water to air. At a flat interface no onset of Marangoni convection could be detected, probably due to some surface contamination. After some solution was released from the container, giving a curved gas/liquid interface, convection started immediately and roll cells developed. This led to the contention that interfacial movements due to surface tension gradients can be divided into macroscale convection and microscale convection (Dijkstra and Lichtenbelt, 1988). Macroscale convection originates from a macroscopic asymmetry of the bulk phase, while microscale convection is caused by hydrodynamic instabilities in the system. This division is connected only to the onset of the convection and not to its final state. Although the onset of the Marangoni convection during the Space-Lab flight was connected to macroscale effects introduced by the curved surface (Dijkstra and Lichtenbelt, 1988), Hoefsloot *et al.* (1990a, b) have revealed that the stability parameters for microscale convection are dependent on the curvature of the interface too.

During two flights with unmanned sounding rockets (1987 and 1988), the influence of interface curvature on Marangoni convection was studied. In several containers, filled with an acetone-in-water solution, air was blown between small glass pipes, creating air bubbles of different diameters. Acetone evaporates from the liquid to the gas. Inhomogeneities in the mass transfer give rise to the onset of Marangoni convection. The sounding rocket launches took place from the ESA basis in Kiruna (Sweden) and were managed by the Swedish Space Corporation under the MASER program (Material Science Experiment Rocket). During these campaigns, a rocket was launched nearly vertically, and during its flight outside the atmosphere, very low levels of gravity could be reached. The duration of the microgravity time was about 7 min and the mean g levels during the flights were of the order of 10^{-4} m/s^2. Additional experiments were performed by us during a series of NASA parabolic flights. During these flights an airplane, fully equipped as laboratory, flies in large parabolas providing g levels in the order of 10^{-2} m/s^2 and microgravity time of about 25 s.

In Section 2 the experimental setup is described. The observed liquid flow patterns for several bubble sizes and air flow rates through the bubble are discussed in Section 3. In Section 4 an explanation is put forward for the difference in liquid flow if the air flow rate through the bubble is changed. In Section 5 a mathematical formulation is stated, with a variable mass transfer coefficient along the interface to take inhomogeneous evaporation into account. The equations for the liquid flow and mass diffusion are discretized and the discrete equations are solved numerically using an alternating-direction implicit method. Section 5 ends with some remarks about the reliability of the numerical algorithm. In Section 6 the numerical results are presented. Parameters like the

‡Author to whom correspondence should be addressed.

Biot number, the Schmidt number and the interface curvature are varied to investigate their influence on the streamline pattern. In Section 7 some general conclusions are drawn.

2. DESCRIPTION OF THE EXPERIMENT

All air bubble experiments were performed in containers with a cylindrical shape as shown in Fig. 1. The inner radius was 20 mm and the inner depth 40 mm and they were filled with a 3% acetone-in-water solution. At the beginning of the experiment the container was completely filled with the liquid, but when microgravity was reached an air bubble was created in each container between an air inlet and an air outlet. In Fig. 2 the growth of the bubble is shown; the air flow is from left to right. The acetone transfers from the liquid to the gas phase. The air flow through the bubble removes the acetone and prevents the bubble from becoming saturated. After leaving the bubble, the acetone is stripped from the air by an active carbon filter and the air is reused. By varying the distance between the air inlet and the air outlet, air bubbles of different sizes could be created. The distances used were 3, 5 and 7 mm; consequently, different curvatures of the gas/liquid interface occurred in the containers. To visualize the fluid flow, silver-coated microballoons with matched density were added to the liquid. The flow was recorded by a video camera. During the sounding rocket flights, there was a TV link between the rocket and the ground station.

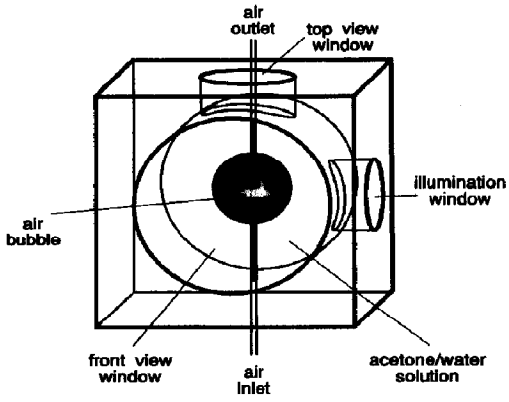

Fig. 1. Experimental setup.

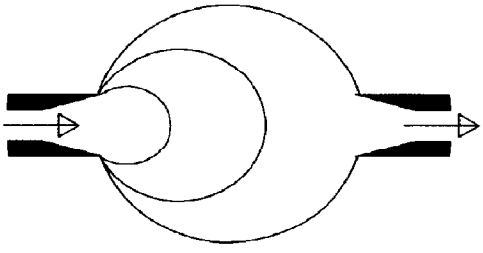

Fig. 2. Air bubble formation between inlet and outlet pipes.

At the ground station the signal was recorded on a video tape. During the parabolic flights, the experiments were recorded directly on a video tape.

The influence of the air flow through the bubble on the convective flow pattern has been investigated during the parabolic flights. The experimental setup was changed in such a way that the air flow rate could be controlled manually by a fine metering valve.

3. EXPERIMENTAL RESULTS

During the first sounding rocket flight (MASER 1), an air bubble with a diameter of 5 mm was created approximately every 7 s in a single container. From the time rate of creation of the bubble (0.2 s) the flow rate of the gas could be derived (0.3 cm^3/s). It was clearly visible that strong Marangoni convection occurred and that the onset was very fast ($\ll 1$ s). The liquid velocities at the interface were typically in the order of 6 mm/s. Figure 3 shows schematically the convective pattern observed. In a two-dimensional projection four stable vortices could be seen. From experiments during the MASER 2 flight it became plausible that these vortices are part of two tori. A detailed description of the MASER 1 experiment and its results is given by Dijkstra and Lichtenbelt (1988).

In the MASER 2 experiment three containers were involved, all filled with a 3% acetone-in-water solution. In each container the distance between air inlet and air outlet was different, resulting in bubble sizes of 3, 5 and 7 mm, respectively. So, the curvature of the interface is different for the three experiments. The bubbles remained stable for several minutes, providing an opportunity to study also longer-term effects. For the 3 and 7 mm bubbles views from two sides were obtained, while for the 5 mm bubble only a view from one side was recorded. The air flow rate was 2 cm^3/s for all three experiments, which is much larger than the flow rate in the MASER 1 experiment.

The 7 mm *bubble*

The Marangoni convection started very fast: after formation of the bubble, the liquid flow started immediately. The behavior of the tracer particles was very characteristic of surface-tension-driven convection. The particles approach the interface with a relatively small velocity but at the interface the particle is suddenly accelerated. After this acceleration, the particles leave the interface and decelerate in the bulk.

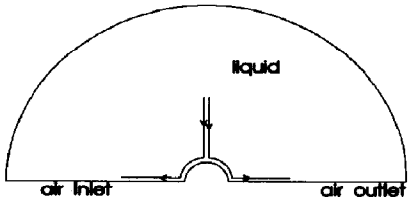

Fig. 3. Sketch of liquid flow pattern observed during MASER 1 experiment.

The largest velocities occur at the interface; for this experiment they were approximately 3 cm/s. The convective pattern was very stable and did not change during the entire period of microgravity. In Fig. 4 the flow pattern around the 7 mm bubble is presented schematically.

The flow profiles of the MASER 1 experiment were very symmetrical, but this was apparently not the case for the MASER 2 experiment. From Fig. 4 it can be seen that the center of the roll cell is not at the same axial position as the center of the bubble.

The 5 mm *bubble*

The two-dimensional view of the 5 mm bubble provided an almost identical picture to that of the 7 mm bubble. The maximum velocities were also in the order of 3 cm/s.

The 3 mm *bubble*

The bubble with a diameter of 3 mm showed a completely different behavior. The onset of convection was slower than in the other experiments and visible convection started only several seconds after the formation of the bubble. Moreover, the convection pattern was not stable and, although sometimes tori could be detected, frequently a 'flow source' at the interface emerged. Liquid was drawn tangentially towards this 'source point' and flowed with a high velocity perpendicular to the interface, from the source point towards the wall of the container. Not only the convective pattern changed frequently but also the shape of the air bubble was not constant throughout the whole experiment. It changed between a spherical and a cylindrical shape. Since the flow rate was not monitored, it is possible that the flow rate through the bubble was not constant. This might explain the strange behavior of the 3 mm bubble.

From the MASER 2 flight only the overall results could be obtained because the TV link was very poor and, therefore, no accurate tracking of the tracer particles was possible. The g levels as well as the isothermal conditions were satisfactory during both the MASER 1 and the MASER 2 flight (SAAB SPACE, 1988).

The difference observed in flow pattern around the 5 mm bubble during the MASER 1 and MASER 2 campaign led to the contention that the air flow through the bubble is also an important parameter for the onset of Marangoni convection. Although the momentum transferred from the flowing air to the liquid is very small compared to the tangential stresses created by the Marangoni effect, the velocity of the air influences the mass transfer boundary layer in the gas phase. This effect has been investigated in parabolic flights (75 periods of 25 s experimental time at microgravity each). During these flights, the flow rate through the bubble was varied and the onset of the convection was recorded. Due to experimental constraints and the less perfect level of microgravity (0.01 g) the air bubbles were not exactly spherical any more.

At air flows larger than 2 cm^3/s the flow in most of the experiments was similar to that observed during the MASER 2 experiments. The flow profile had the shape of a single torus and the liquid flow at the interface was in the direction from the gas inlet towards the gas outlet. When the air flow was small (of the order of 0.1 cm^3/s) the flow profile showed also one torus, but the liquid at the interface was moving in the opposite direction compared to the cases with air flow rate larger than 2 cm^3/s (Fig. 5).

At intermediate air flows, convective patterns with a double torus developed as sketched in Fig. 6.

To be sure that the drag from the air did not result in a liquid flow, also dummy experiments were performed in which there was no acetone in the water

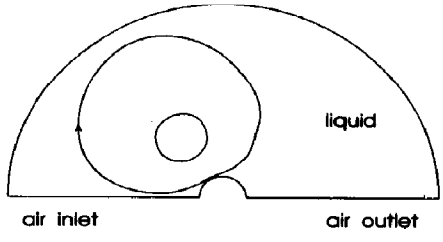

Fig. 5. Sketch of flow pattern of the liquid at low air flow rates through the bubble.

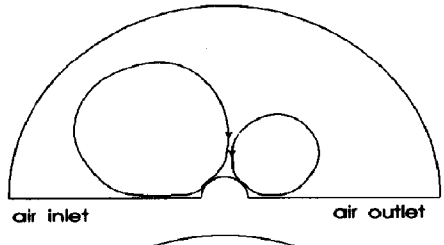

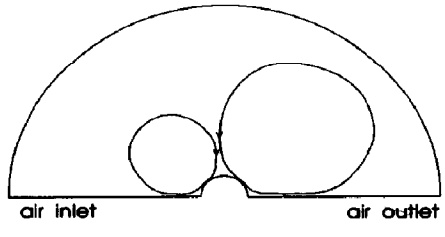

Fig. 6. Sketch of liquid flow patterns at intermediate air flow rates.

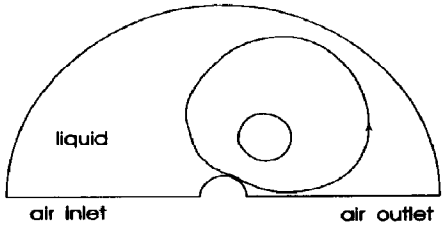

Fig. 4. Sketch of liquid flow pattern around the 7 mm bubble during the MASER 2 experiment.

(and no Marangoni effects were expected). The result was that even at the highest possible air flow rate the liquid remained motionless. Another phenomenon observed was that at larger bubble sizes the flow looked more vigorous. This might be due to the fact that a larger interfacial area allows more energy to be transferred to the liquid.

The conclusion of the sounding rocket flights was that in all experiments Marangoni convection was detected. However, the convective pattern in the liquid depended strongly on the air flow rate through the bubble. In the next section an explanation of this dependency will be given.

4. QUALITATIVE EXPLANATION OF THE EXPERIMENTAL RESULTS

The liquid flow is caused by local differences in the evaporation of acetone from the liquid into the air bubble. To understand the experimental results, one should realize that due to the fact that the bubble is ventilated the mass transfer resistance is not uniform along the interface between the bubble and the liquid. The air flow through the bubble has been computed with the help of the PHOENICS flow package. If the air flow is larger than 0.17 cm^3/s (that is, the Reynolds number based on the average flow velocity exceeds the value 6), recirculation will occur in the bubble (see Fig. 7). The vortical region will become larger when the air flow increases.

To obtain an impression of the influence of the air flow on the evaporation of the acetone, also a steady convection/diffusion problem was solved with PHOENICS. Figure 8 shows the computational domain, composed of a liquid-phase region and a gas-phase region in an axisymmetrical coordinate system. In the liquid region no motion is assumed to occur; so in that region only a diffusion equation is solved. In the gas phase we have solved the Navier–Stokes equations combined with a convection/diffusion equation. To make sure that the problem possesses a steady solution, the concentration at the outer boundaries (6, 7, 8) of the liquid region is kept constant (equal to unity). The numerical grid generated by the PHOENICS package is shown in Fig. 9. The convergence of this calculation is fast and the results seem to be reliable. In Fig. 10 the computed solute concentration in the liquid at the gas/liquid interface is shown.

It can be seen that the interfacial concentration for an air flow with $Re = 1$ (0.028 cm^3/s) increases from inlet to outlet. Therefore the direction of the liquid flow at the interface due to surface tension gradients will be from outlet towards inlet, which is exactly the flow pattern observed for small air flow rates (see Fig. 5). For an intermediate flow rate of $Re = 15$ (0.43 cm^3/s) the concentration first increases and then decreases. This leads to a liquid flow at the interface as sketched in Fig. 6. For a larger air flow $Re = 30$ (0.86 cm^3/s) the concentration along the interface decreases monotonously, causing a convective pattern where the liquid flow at the interface is from gas inlet towards gas outlet. The computations agree qualitatively with the experimental results and have shown that the evaporation is not uniform along the interface. The type of nonuniformity depends on the air flow rate through the bubble. At small (large) air flow rates the mass transfer resistance in the gas phase is small (large) near the inlet and large (small) near the outlet, whereas for intermediate air flow rates the resistance in the gas phase is relatively small near the inlet and outlet, with a higher value in between. In the mathematical model the effect of the various flow regimes within the bubble on the mass transfer across the interface will be simulated by prescribing

Fig. 7. Computed flow pattern of the air in the bubble with $Re = 15$.

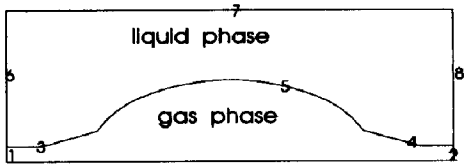

Fig. 8. Setup for the PHOENICS package. 1—air inlet; 2—air outlet; 3—inlet tube; 4—outlet tube; 5—air/liquid interface; 6, 7, 8—boundaries at which the concentration is kept constant.

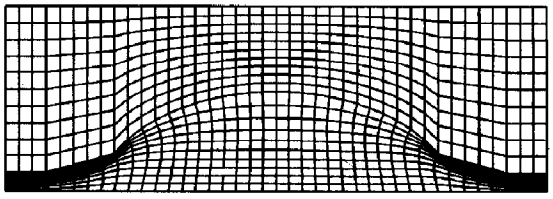

Fig. 9. The grid generated by the PHOENICS package.

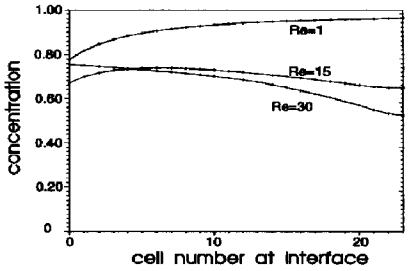

Fig. 10. Computed solute concentration at the gas/liquid interface. Cell number 0 is nearest to the air inlet and cell number 23 is nearest to the gas outlet.

a gas/liquid mass transfer coefficient which is a suitably chosen function of the location along the interface.

5. THE THEORETICAL MODEL

To explain the observed flow patterns a mathematical model is formulated based on axisymmetric flow of a Newtonian viscous liquid bounded by two concentric spherical surfaces, one with radius a (gas bubble/liquid interface) and the other with radius $a + H$ (container boundary) (see Fig. 11). The inlet of the gas flow in the bubble corresponds to $\theta = \pi$, the outlet to $\theta = 0$. We have chosen not to combine the governing equations in the gas phase and the fluid phase because the computing time would become excessive. Even with our dedicated code for the fluid phase one computer run extending over 30 s physical time (6000 time steps) took about 12 h CPU time on a Cyber 962 mainframe. Moreover, the PHOENICS code does not provide the necessary Marangoni boundary conditions.

The governing equations in the liquid region are the Navier–Stokes equations and the convection/diffusion equation, all of them being expressed in spherical coordinates. Introducing the nondimensional radial coordinate r, time t, stream function Ψ, vorticity ω, and solute concentration c by scaling their dimensional counterparts with H, H^2/ν, $H\nu$, ν/H^2 and c_{in} respectively, where ν is the kinematic viscocity and c_{in} the initial solute concentration, the following set of equations in the liquid region $a/H \leqslant r \leqslant 1 + a/H$, $0 \leqslant \theta \leqslant \pi$ has to be solved [see Myshkis *et al.* (1987)]:

$$\frac{\partial\omega}{\partial t} = \frac{\partial^2\omega}{\partial r^2} + \frac{1}{r^2}\frac{\partial^2\omega}{\partial\theta^2} + \frac{2}{r}\frac{\partial\omega}{\partial r} + \frac{\cot\theta}{r^2}\frac{\partial\omega}{\partial\theta} - \frac{1}{r^2\sin^2\theta}\omega - \frac{1}{r^2\sin\theta}\left[\frac{\partial\Psi}{\partial r}\frac{\partial\omega}{\partial\theta} - \frac{\partial\Psi}{\partial\theta}\frac{\partial\omega}{\partial r} - \omega\left(\cot\theta\frac{\partial\Psi}{\partial r} - \frac{1}{r}\frac{\partial\Psi}{\partial\theta}\right)\right] \quad (1)$$

$$\omega = \frac{1}{r\sin\theta}\left[\frac{\partial^2\Psi}{\partial r^2} + \frac{1}{r^2}\frac{\partial^2\Psi}{\partial\theta^2} - \frac{\cot\theta}{r^2}\frac{\partial\Psi}{\partial\theta}\right] \quad (2)$$

$$\frac{\partial c}{\partial t} = \frac{1}{r^2\,Sc}\left[\frac{\partial}{\partial r}\left(r^2\frac{\partial c}{\partial r}\right) + \frac{1}{\sin\theta}\frac{\partial}{\partial\theta}\left(\sin\theta\frac{\partial c}{\partial\theta}\right)\right] + \frac{1}{r^2\sin\theta}\left(\frac{\partial\Psi}{\partial\theta}\frac{\partial c}{\partial r} - \frac{\partial\Psi}{\partial r}\frac{\partial c}{\partial\theta}\right) \quad (3)$$

where the Schmidt number Sc is defined as ν/D, D being the diffusion coefficient in the liquid. The nondimensional velocity components v_r and v_θ are related to Ψ by

$$v_r = -\frac{1}{r^2\sin\theta}\frac{\partial\Psi}{\partial\theta}, \qquad v_\theta = \frac{1}{r\sin\theta}\frac{\partial\Psi}{\partial r}. \quad (4)$$

At time $t = 0$ the initial conditions are

$$\Psi = \omega = 0, \qquad c = 1. \quad (5)$$

At the solid container wall $r = 1 + a/H$ the boundary conditions

$$\Psi = 0, \quad \omega = \frac{1}{r\sin\theta}\frac{\partial^2\Psi}{\partial r^2}, \quad \frac{\partial c}{\partial r} = 0 \quad (6)$$

should be satisfied, whereas at the symmetry axis ($\theta = 0$, $\theta = \pi$) we have

$$\Psi = \omega = \frac{\partial c}{\partial\theta} = 0. \quad (7)$$

The three boundary conditions at the gas/liquid interface $r = a/H$ are as follows. First, it is assumed that the gas bubble remains spherical; so

$$\Psi = 0 \quad \text{at } r = a/H. \quad (8)$$

Secondly, we have the mass transfer condition

$$\frac{\partial c}{\partial r} = Bi(\theta)c \quad \text{at } r = a/H \quad (9)$$

where the Biot number Bi is defined as $k(\theta)H/D$, k being a θ-dependent mass transfer coefficient. By making appropriate choices of Bi as a function of θ, we can model the nonuniformity of the evaporation at the interface resulting from the various flow regimes within the bubble. Finally, the tangential stress balance reads (Myshkis *et al.*, 1987)

$$r\frac{\partial}{\partial r}\left(\frac{v_\theta}{r}\right) = \frac{1}{r}\frac{Ma}{Sc}\frac{\partial c}{\partial\theta} \quad \text{at } r = a/H \quad (10)$$

or, in terms of Ψ and ω,

$$\omega r = \frac{Ma}{Sc}\frac{\partial c}{\partial\theta} + \frac{2}{r\sin\theta}\frac{\partial\Psi}{\partial r} \quad \text{at } r = a/H. \quad (11)$$

The Marangoni number is defined as

$$Ma = -\frac{(d\gamma/d\tilde{c})c_{in}H}{\mu D} \quad (12)$$

where μ is the dynamic viscosity and $d\gamma/d\tilde{c}$ is the derivative of the surface tension γ with respect to the dimensional solute concentration $\tilde{c}$. The usual assumption will be made to take $d\gamma/d\tilde{c}$ equal to a negative constant.

To solve this initial/boundary value problem numerically, we used an alternating-direction-implicit (ADI) finite-difference method. The discretization scheme for this method leads, after linearization, to

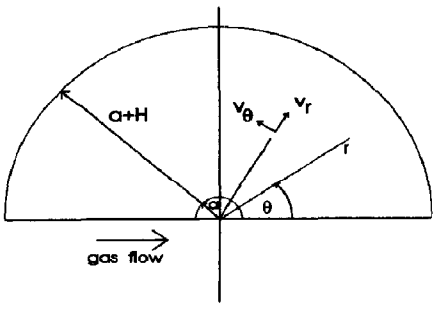

Fig. 11. Definition sketch for the convection/diffusion flow problem in the liquid.

Table 1. The maximum of the stream function (Ψ_{max}) and the velocity at the interface at $\theta = 135°$ (denoted by V_{135}) at $t = 0.01$ for three $\theta \times r$ grids (41×41, 81×81, 161×162) and three values of Δt (5×10^{-5}, 2.5×10^{-5}, 1.25×10^{-5})

Grid	41×41		81×81		161×161	
Δt	Ψ_{max}	V_{135}	Ψ_{max}	V_{135}	Ψ_{max}	V_{135}
5×10^{-5}	0.0165	2.0611	0.0129	1.6748	0.01212	1.5858
2.5×10^{-5}	0.0165	2.0678	0.0130	1.6769	0.01215	1.5875
1.25×10^{-5}	0.0165	2.0712	0.0130	1.6775	0.01216	1.5880

matrix equations involving coefficient matrices with a band structure of band width 3, that can be solved in a relatively easy manner. The time-discretized form of the basic equations [eqs (1)–(3)] is [see Myshkis *et al.* (1987)]

$$P\frac{\omega^{m+1/2}-\omega^m}{\Delta t}=\frac{1}{2}\left(Q\frac{\partial^2\omega^{m+1/2}}{\partial\theta^2}+A\frac{\partial\omega^{m+1/2}}{\partial\theta}\right)+\frac{1}{2}\left(P\frac{\partial^2\omega^m}{\partial r^2}+B\frac{\partial\omega^m}{\partial r}\right)+\frac{C}{4}(\omega^{m+1/2}+\omega^m) \quad (13)$$

$$P\frac{\omega^{m+1}-\omega^{m+1/2}}{\Delta t}=\frac{1}{2}\left(Q\frac{\partial^2\omega^{m+1/2}}{\partial\theta^2}+A\frac{\partial\omega^{m+1/2}}{\partial\theta}\right)+\frac{1}{2}\left(P\frac{\partial^2\omega^{m+1}}{\partial r^2}+B\frac{\partial\omega^{m+1}}{\partial r}\right)+\frac{C}{4}(\omega^{m+1/2}+\omega^{m+1}) \quad (14)$$

$$P_1\frac{\Psi^{n+1/2}-\Psi^n}{\tau}=\frac{1}{2}\left(\sin\theta\frac{\partial^2\Psi^{n+1/2}}{\partial\theta^2}-\cos\theta\frac{\partial\Psi^{n+1/2}}{\partial\theta}\right)+\frac{1}{2}\left(r^2\sin\theta\frac{\partial^2\Psi^n}{\partial r^2}-r^3\sin^2\theta\omega^{m+1}\right) \quad (15)$$

$$P_1\frac{\Psi^{n+1}-\Psi^{n+1/2}}{\tau}=\frac{1}{2}\left(\sin\theta\frac{\partial^2\Psi^{n+1/2}}{\partial\theta^2}-\cos\theta\frac{\partial\Psi^{n+1/2}}{\partial\theta}\right)+\frac{1}{2}\left(r^2\sin\theta\frac{\partial^2\Psi^{n+1}}{\partial r^2}-r^3\sin^2\theta\,\omega^{m+1}\right) \quad (16)$$

$$P_2\frac{c^{m+1/2}-c^m}{\Delta t}=\frac{1}{2}\left[\frac{1}{Sc}\frac{\partial}{\partial\theta}\left(\sin\theta\frac{\partial c^{m+1/2}}{\partial\theta}\right)-\frac{\partial\Psi^{m+1}}{\partial r}\frac{\partial c^{m+1/2}}{\partial\theta}\right]+\frac{1}{2}\left[\frac{\sin\theta}{Sc}\frac{\partial}{\partial r}\left(r^2\frac{\partial c^m}{\partial r}\right)+\frac{\partial\Psi^{m+1}}{\partial\theta}\frac{\partial c^m}{\partial r}\right] \quad (17)$$

$$P_2\frac{c^{m+1}-c^{m+1/2}}{\Delta t}=\frac{1}{2}\left[\frac{1}{Sc}\frac{\partial}{\partial\theta}\left(\sin\theta\frac{\partial c^{m+1/2}}{\partial\theta}\right)-\frac{\partial\Psi^{m+1}}{\partial r}\frac{\partial c^{m+1/2}}{\partial\theta}\right]+\frac{1}{2}\left[\frac{\sin\theta}{Sc}\frac{\partial}{\partial r}\left(r^2\frac{\partial c^{m+1}}{\partial r}\right)+\frac{\partial\Psi^{m+1}}{\partial\theta}\frac{\partial c^{m+1}}{\partial r}\right] \quad (18)$$

with

$$P=r^2\sin^2\theta,\quad P_1=r^3\sin^2\theta,\quad P_2=r^2\sin\theta$$

$$Q=\sin^2\theta,\quad A=\sin\theta\left(\cos\theta-\frac{\partial\Psi}{\partial r}\right)$$

$$B=\sin\theta\left(2r\sin\theta-\frac{\partial\Psi}{\partial\theta}\right)$$

$$C=\cos\theta\frac{\partial\Psi}{\partial r}-\frac{\sin\theta}{r}\frac{\partial\Psi}{\partial\theta}-1.$$

The superscript m denotes the time level $t = m\Delta t$. In eqs (15) and (16) a pseudotime discretization has been introduced with time step τ and level counter n. All derivatives with respect to the spatial variables r and θ occurring in the basic equations and in the boundary conditions have been replaced by second-order differences. An equidistant grid has been used in the θ-direction, whereas in the r-direction a nonuniform grid has been used with a higher density of grid points near the interface $r = a/H$, where the gradients of concentration and velocity are large. The nonequidistant grid points have been defined as

$$r_i = a/H + 0.9(i/N)^2 + 0.1(i/N),\ i = 0, 1, \ldots, N.$$

The numerical computation is carried out as follows. Assuming that Ψ, ω and c are known at time level m, first the value $\omega^{m+1/2}$ at the intermediate level $m + 1/2$ is computed from eq. (13), and using this value of $\omega^{m+1/2}$ in eq. (14), the value of ω^{m+1} is computed. Next, Ψ at level $m + 1$ is computed iteratively from eqs (15) and (16) with n as iteration counter and using the stop criterion $|\Psi^n - \Psi^{n+1}| < 10^{-6}$. During this iteration, the pseudotime step τ is not kept fixed, but can be enlarged when n increases, thus saving computer time. Finally, the computed value Ψ^{m+1} is used in eqs (17) and (18) to compute subsequently the concentration values $c^{m+1/2}$ and c^{m+1}. At this stage Ψ, ω and c are known at time level $m + 1$; so m can now be changed into $m + 1$ and the procedure is repeated. This method is probably not the most cost-efficient one, but it is reliable and works well, also for large values of Ma and Sc.

The correctness of the numerical algorithm has been checked in several ways. First, theoretical convergence of the method, which is $O(\Delta t, \Delta r^2, \Delta\theta^2)$, has been checked (see Table 1). This table presents the maximum of the stream function (Ψ_{max}) and the velocity at the interface at $\theta = 135°$ denoted by V_{135}) at $t = 0.01$, which corresponds to a physical time for 4 s. The parameter values were $Ma = 10^6$, $Sc = 10^3$, $Bi(\theta) = 12 - 4\sin\theta$ (the parameter choice will be dis-

cussed later). The values given in Table 1 for three $\theta \times r$ grids (41×41, 81×81, 161×161) and three values of Δt (5×10^{-5}, 2.5×10^{-5}, 1.25×10^{-5}) indeed show the desired convergence behavior. Table 2 shows that the convergence is particularly dependent on the number of grid points in radial direction. For a 21×161 grid and $\Delta t = 5 \times 10^{-5}$ the error in the velocity at the interface (which is the most sensitive test) is about 3%.

Secondly, for $a/H \gg 1$ curvature effects will be absent and our results can be compared with those for a plane liquid layer obtained by Dijkstra and Lichtenbelt (1988). The comparison yielded very favorable results, the streamline plots being very similar and the values of Ψ_{max} differing by less than 2%.

When the numerical computation is pursued for much longer time than above, some numerical instability in the form of oscillations (wiggles) becomes visible in the result. This is due to increasing flow velocities as time advances, and this leads to a larger ratio between the convective and diffusive terms in the equations. The occurrence of numerical wiggles in the solution is a familiar phenomenon under these circumstances. To suppress this undesirable effect, the standard method is to reduce the step sizes. However, in the situations considered this would lead to unacceptably large computation times. Therefore, the numerical results presented in the next section have been obtained on the basis of the following compromise: the weight of the diffusive terms has been increased by choosing the Schmidt number Sc in the range from 50 to 200 (instead of the actual value $Sc = 787$ for

Table 2. The velocity at the interface at $\theta = 135°$ calculated with 21×41, 21×81 and 21×161 grids and with $\Delta t = 5 \times 10^{-5}$

Grid $\theta \times r$	21×41	21×81	21×161
Δt	V_{135}	V_{135}	V_{135}
5×10^{-5}	2.0724	1.6742	1.5839

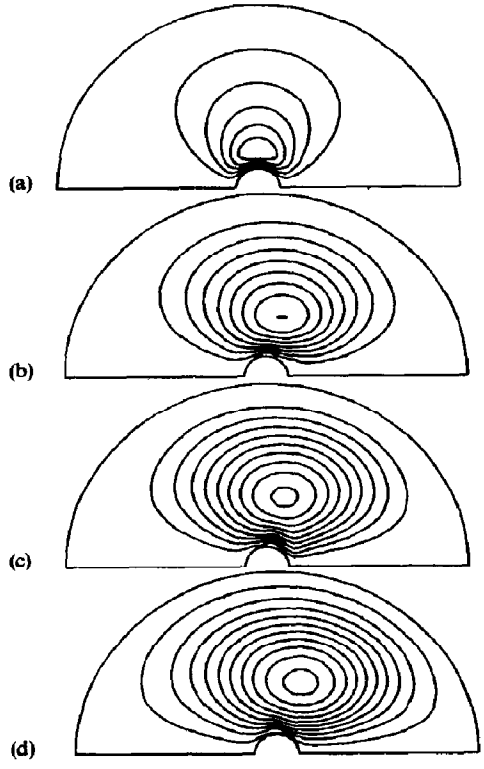

Fig. 12. Contour plots of the stream function after 1 s (a), 10 s (b), 20 s (c) and 30 s (d), with parameters $Ma = 10^5$, $a/H = 0.125$, $Sc = 100$ and $Bi(\theta) = 55 - 50\theta/\pi$. The flow is from left to right at the interface. The extreme values of the stream function Ψ are given in the following table:

	$t = 0$	$t = 1$	$t = 10$	$t = 20$	$t = 30$
Ψ_{max}	0	0	0	0	0
Ψ_{min}	0	− 0.0481	− 0.3216	− 0.3705	− 0.3963

acetone in water) and the step sizes have been chosen as $\Delta\theta = 1/60$, $\Delta r = 1/240$ and $\Delta t = 1.25 \times 10^{-5}$. As will be shown later, changes in the Schmidt number affect only the absolute value of the velocities but they do not change the shape of the stream lines.

The chosen variation of the Biot number between the values 5 and 55 agrees with the experimental conditions. The boundary conditions in the fluid domain expressed in the Biot number are qualitatively obtained from the results of the simulations in the gas phase as presented in Fig. 10. For Ma a value of 10^5 has been used. Although for the systems used in our experiment (3% acetone in water), in principle, Marangoni numbers of 10^8 can be achieved, in practical situations these numbers are always some orders of magnitude smaller due to some slight contamination. Further, we have taken $H = 0.02$ m, $\nu = 10^{-6}$ m^2/s and, in most of the computations, $a/H = 0.125$.

6. NUMERICAL RESULTS

The majority of our numerical results will be presented in the form of a sequence of contour plots of the stream function Ψ for various values of the physical time t. At time $t = 0$ the liquid is motionless ($\Psi = 0$ everywhere) and the solute concentration is uniform throughout the liquid. At the boundary of the liquid region Ψ equals zero; so the maximum and/or minimum value of Ψ gives a good indication of the relative order of magnitude of the flow velocities.

In Figure 12(a)–(d) the time evolution of the flow for parameters $Ma = 10^5$, $a/H = 0.125$, $Sc = 100$ and $Bi(\theta) = 55 - 50\theta/\pi$ is presented. This choice of $Bi(\theta)$ simulates relatively large air flows through the bubble for which the mass transfer resistance in the gas phase is large near the inlet ($\theta = \pi$) and small near the outlet ($\theta = 0$). The liquid at the interface flows in the direc-

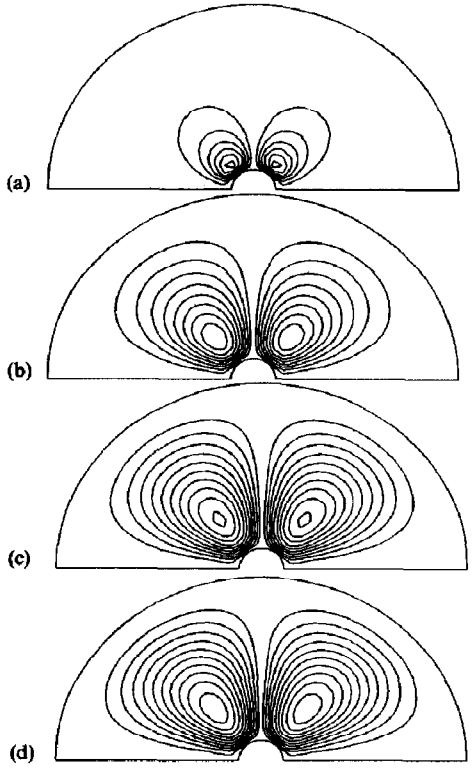

Fig. 13. Contour plots of the stream function after 1 s (a), 10 s (b), 20 s (c) and 30 s (d), with parameters $Ma = 10^5$, $a/H = 0.125$, $Sc = 100$ and $Bi(\theta) = 25 - 20\sin\theta$. The flow at the interface is from the center towards left and right. The extreme values of the stream function Ψ are given in the following table:

	$t = 0$	$t = 1$	$t = 10$	$t = 20$	$t = 30$
Ψ_{max}	0	0.0263	0.0889	0.1016	0.1068
Ψ_{min}	0	−0.0263	−0.0889	−0.1016	−0.1068

tion from the inlet to the outlet side. The computed flow pattern is seen to be very similar to the one observed in the MASER 2 experiment (see Fig. 4), in which the air flow rate was rather large. Initially, the flow velocities increase quite rapidly. However, after about 20 s the flow changes only very slowly. This can be understood by realizing that the characteristic time for the diffusion process is much smaller than the characteristic time for the liquid flow.

The case of small air flow through the bubble can be modeled by taking $Bi(\theta) = 5 + 50\theta/\pi$, which is complementary to the boundary condition given above. The streamline patterns obtained are mirror images of Fig. 12(a)–(d) with respect to the axis $\theta = \pi/2$, with a corresponding change in the orientation of the liquid flow velocity. This resulting pattern also resembles the experimentally observed pattern (Fig. 5), for which the air flow through the bubble was small.

An intermediate air flow rate is simulated by $Ma = 10^5$, $a/H = 0.125$, $Sc = 100$ and $Bi(\theta) = 25 - 20\sin\theta$. Now a relatively large mass transfer resistance of the gas for $\theta = \pi/2$ and a small one for $\theta = 0$ and $\theta = \pi$ should lead to a flow pattern similar to that in Fig. 3. The computed streamline plots [Fig. 13(a)–(d)] indeed show the expected double torus pattern.

All situations discussed above are typical cases of macroscale convection, because the supposed θ-dependence of Bi immediately leads to a macroscopic inhomogeneity of surface tension along the interface, which is responsible for the onset of the convective motion. If Bi is constant, we have a hydrodynamic stability problem in which a small initial disturbance is required for the onset of the liquid flow (microscale convection). Figure 14 presents the results for $Ma = 10^5$, $a/H = 0.125$, $Sc = 100$ and $Bi(\theta) = 20$. The initial disturbance is chosen to be a constant gradient of c along the interface where $c = 0.9$ at $\theta = 0$ and $c = 1.0$ at $\theta = \pi$. This disturbance results in an initial flow consisting of one large roll cell. This large roll cell starts to break up into smaller cells as can be seen in Fig. 14.

The influence of the Schmidt number was studied by computing the flow patterns for the macroscale case $Ma = 10^5$, $a/H = 0.125$, $Bi(\theta) = 55 - 50\theta/\pi$ with $Sc = 50$ or 200. The streamline plots of Fig. 15 and Fig. 12(d) are all very similar, but the velocity decreases with increasing Schmidt number; see Table 3.

Table 3. The minimum of the stream function for three different Schmidt numbers at $t = 1$ and 10 s

	Ψ_{min} ($t = 1$)	Ψ_{min} ($t = 10$)
$Sc = 50$	− 0.1375	− 0.6300
$Sc = 100$	− 0.0481	− 0.3216
$Sc = 200$	− 0.0183	− 0.1719

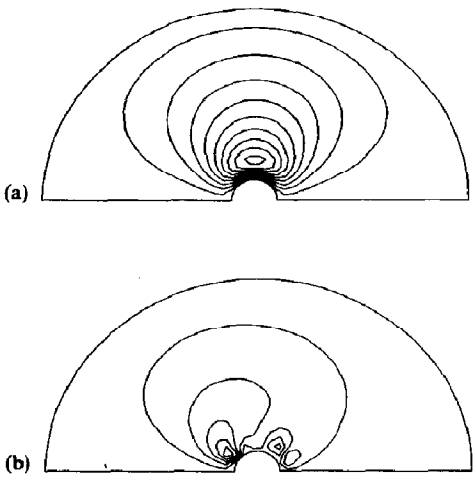

Fig. 14. Contour plots of the stream function for a microscale case (see text) after 1 s (a) and 7.5 s (b), with parameters $Ma = 10^5$, $a/H = 0.125$, $Sc = 100$ and $Bi(\theta) = 20$. The extreme values of the stream function Ψ are given in the following table:

	$t = 0$	$t = 1$	$t = 7.5$
Ψ_{max}	0	0	0.0059
Ψ_{min}	0	− 0.0018	− 0.0119

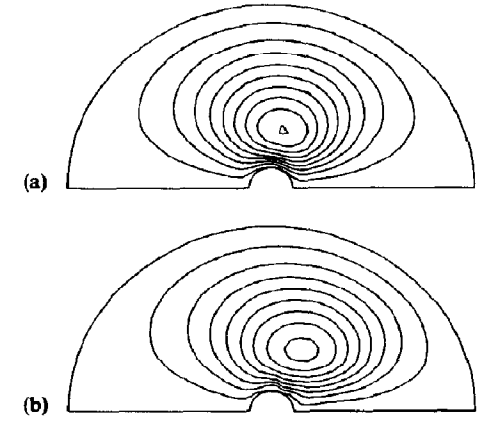

Fig. 15. Contour plots of the stream function after 10 s for $Sc = 50$ (a) and $Sc = 200$ (b), the other parameter values being $Ma = 10^5$, $a/H = 0.125$ and $Bi(\theta) = 55 - 50\theta/\pi$. At $t = 0$ the liquid is motionless and the stream function is zero everywhere. The minimum stream function values for $t = 10$ s are for (a) Ψ_{min} ($Sc = 50$) = − 0.6300 and for (b) Ψ_{min} ($Sc = 200$) = 0.1719.

Another parameter of interest is the curvature parameter a/H. Figure 16(a)–(d) shows the results for $Ma = 10^5$, $Sc = 100$, $Bi(\theta) = 55 - 50\theta/\pi$ and $a/H = 0.075$ (instead of 0.125). The flow patterns are quite similar to those of Fig. 12(a)–(d). In Table 4 we present the values of Ψ_{min}, from which it can be

Table 4. The minimum of the stream function for two different curvatures at $t = 1$, 10, 20 and 30 s

	Ψ_{min} $(t = 1)$	Ψ_{min} $(t = 10)$	Ψ_{min} $(t = 20)$	Ψ_{min} $(t = 30)$
$a/H = 0.125$	− 0.0499	− 0.3216	− 0.3706	− 0.3963
$a/H = 0.075$	− 0.0359	− 0.1820	− 0.2284	− 0.2508

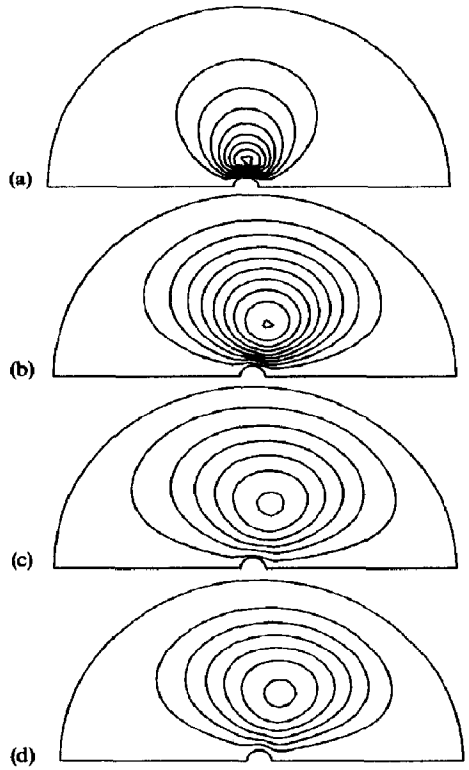

Fig. 16. Contour plots of the stream function after 1 s (a), 10 s (b), 20 s (c) and 30 s (d), with parameters $Ma = 10^5$, $a/H = 0.125$, $Sc = 100$ and $Bi(\theta) = 55 - 50\theta/\pi$. The flow is from left to right at the interface. The extreme values of the stream function Ψ are given in the following table:

	$t = 0$	$t = 1$	$t = 10$	$t = 20$	$t = 30$
Ψ_{max}	0	0	0	0	0
Ψ_{min}	0	− 0.0359	− 0.1820	− 0.2284	− 0.2508

concluded that the flow velocities decrease as a/H decreases.

It is also possible for macroscale and microscale effects to occur simultaneously. In the earlier macroscale cases the gradient of the Biot number is chosen in such a way that the large cell structure of the flow remains intact. However, if this gradient is chosen to be smaller, local hydrodynamical instability (microscale convection) may cause smaller roll cells to develop. This is shown in Fig. 17, where $Ma = 10^5$, $a/H = 0.125$, $Sc = 100$ and $Bi(\theta) = 16 - 6 \sin \theta$. Here one can see two additional small roll cells which have emerged after 20 s near the plane of symmetry.

7. CONCLUDING REMARKS

The main conclusion of our study is that the experimentally observed liquid flow pattern resulting from Marangoni instability round a ventilated air bubble can be adequately described only by assuming nonhomogeneous mass transfer across the gas/liquid interface, that is, the Biot number does not have the same value for all points of the interface. A Biot number varying gradually along the interface introduces a macroscale effect and leads to the observed stable flow patterns consisting of one or two large cells (macroconvection). If the Biot number is taken to

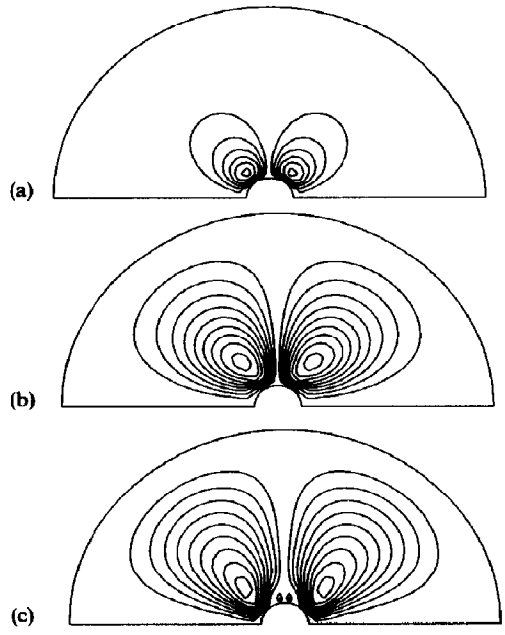

Fig. 17. Contour plots of the stream function after 1 s (a), 10 s (b) and 20 s (c), with $Ma = 10^5$, $a/H = 0.125$, $Sc = 100$ and $Bi(\theta) = 16 - 6\sin\theta$. At $t = 0$ the liquid is motionless and the stream function is zero everywhere. The maximum stream function value for $t = 1$ s is $\Psi_{max} = 0.0066$, for $t = 10$ s, $\Psi_{max} = 0.0378$ and for $t = 20$ s, $\Psi_{max} = 0.0386$.

be constant, the model corresponds to a hydrodynamic stability problem where some small initial perturbation is needed to give convection a start (microconvection). If the perturbation is such that initially some large cells emerge, these cells will first break up into a larger number of small cells. From this fact one can conclude that the experimentally observed flow patterns were not due to hydrodynamical instability of the system but were due to macroeffects. A difference of practical importance between microconvection and macroconvection is that the liquid flow velocities are much larger in the latter case, leading to entirely different mixing behavior.

In most practical situations (for example, in the case of packed columns) mass transfer rates will not be uniform and, consequently, spatially varying Biot numbers should be introduced for a proper simulation of the effect of Marangoni convection on the performance of mass transfer equipment.

NOTATION

a	bubble radius
Bi	Biot number
c	concentration
D	diffusion coefficient
H	liquid depth
k	mass transfer coefficient
Ma	Marangoni number
Re	Reynolds number
r	radial coordinate
Sc	Schmidt number
t	time
v_r	radial velocity
v_θ	angular velocity

Greek letters

γ	surface tension
θ	angular coordinate
ν	viscosity
τ	pseudotime step
Ψ	stream function
ω	vorticity

Superscipts

m	time level
n	iteration counter

Subscripts

in	initial
max	maximum
min	minimum

REFERENCES

Dijkstra, H. A. and Lichenbelt, J. H., 1988, Mass transfer driven Marangoni convection under micro-gravity. *Appl. Microgravity Technol.* **1**, 180–187.

Hoefsloot, H. C. J. and Hoogstraten, H. W., 1989, Marangoni instability in spherical shells. *Appl. Microgravity Technol.* **2**, 106–108.

Hoefsloot, H. C. J., Hoogstraten, H. W., Hoven, A. and Janssen, L. P. B. M., 1990a, Marangoni instability in a liquid layer bounded by two coaxial surfaces. *Appl. Sci. Res.* **47**, 1–21.

Hoefsloot, H. C. J., Hoogstraten, H. W. and Janssen, L. P. B. M., 1990b, Marangoni instability in a liquid layer confined between two concentric spherical surfaces. *Appl. Sci. Res.* **47**, 357–377.

Hoefsloot, H. C. J. and Janssen, L. P. B. M., 1989, Maser-2 report, in *Experiment Reports from Flight Opportunities on Maser-1 and -2 supported by ESA* (Edited by J. P. B. Vreeburg). National Aerospace Laboratory NLR, Amsterdam.

Hoefsloot, H. C. J. and Janssen, L. P. B. M., 1989, Marangoni convection mass transfer, in *Microgravity Experiments during Parabolic Flights of KC-135 Aircraft*, sixth ESA campaign August 1988 (Edited by A. Gonfalone, V. Pletser and D. Frimout). ESTEC, Noordwijk.

Lichtenbelt, J. H., 1986, Improvement of flight hardware and isothermal Marangoni convection under micro-gravity conditions. *Adv. Space Res.* **5**, 97–100.

Lichtenbelt, J. H., Drinkenburg, A. A. H. and Dijkstra, H. A., 1986, Marangoni convection and mass transfer from the liquid to the gas phase. *Naturwissenschaften* **73**, 356–359.

Myshkis, A. D., Babskii, V. G., Kopachevskii, N. D., Slobozhanin, L. A. and Tyuptsov, A. D., 1987, *Low-gravity Fluid Mechanics*. Springer, Berlin.

Nield, D. A., 1964, Surface tension and buoyancy effects in cellular convection. *J. Fluid Mech.* **19**, 341–352.

Pearson, J. R. A., 1958, On convection cells induced by surface tension. *J. Fluid Mech.* **4**, 489–500.

SAAB SPACE, 1988, Final report ESA microgravity modules for MASER 2. European Space Agency contract report, Göteborg.